

Phase formation in iron silicide nanodots grown by reactive deposition epitaxy on Si(111)

J. C. González, D. R. Miquita, M. I. N. da Silva, R. Magalhães-Paniago, M. V. B. Moreira, and A. G. de Oliveira
*Departamento de Física, Instituto de Ciências Exatas, Universidade Federal de Minas Gerais, Caixa Postal 702,
 30123-970 Belo Horizonte, MG, Brazil*

(Received 16 December 2009; published 5 March 2010)

The epitaxial growth by reactive deposition of ϵ -FeSi and β -FeSi₂ nanodots on Si(111) is studied as a function of Fe coverage. The nanodots density, size, and strain were analyzed by atomic force microscopy and x-ray diffraction. Almost single phase ϵ -FeSi and β -FeSi₂ were formed at low and high iron coverage, respectively. A ϵ -FeSi to β -FeSi₂ change in phase formation is observed at Fe coverage of 5.5 nm, which is coincident with the coalescence of the nanodots, the relaxation of the strain in both phases and a discontinuous increase of the grain size of the β -FeSi₂ phase. A direct comparison of the diffraction and microscopy data shows that nanodots of different phases also exhibit different shapes, being the ϵ -FeSi (β -FeSi₂) nanodots smaller (larger) and with a low (high) aspect ratio.

DOI: [10.1103/PhysRevB.81.113403](https://doi.org/10.1103/PhysRevB.81.113403)

PACS number(s): 68.37.Ps, 64.70.Nd, 68.55.A-, 81.16.Dn

In recent years, there has been a trend in materials science and engineering toward the development of environmental-friendly materials. Iron silicides are composed of nontoxic and abundant elements. In particular, semiconducting β -FeSi₂ presents a number of advantages for industrial applications due to its excellent physical properties such as a band gap of ~ 0.85 eV,¹ large optical absorption coefficients,² and high Seebeck coefficient.³ This material is a promising material for Si-based optoelectronic devices⁴ and solar cells,⁵ and can be epitaxially grown on Si substrates by reactive deposition epitaxy (RDE) and solid phase epitaxy (SPE).^{6,7} However, thin films grown using these techniques have many defects in the form of misfit dislocations and Si vacancies⁸ and exhibit an indirect band gap,¹ which are important limiting factors for high performance optoelectronic devices and solar cells. Nevertheless, the lattice mismatch between Si and iron silicides can be used as a driving force to produce coherent nanostructures with no misfit dislocations, lattice mismatch strain and direct band gap. Therefore, iron silicide self-assembled nanostructures not only solve part of the issues presented by thin films, but also have great potential for improved optoelectronic devices.

A variety of fabrication methods^{9–14} has been applied to synthesize iron silicides thin films. In the present study, we show that high quality self-assembled iron silicide nanodots can be fabricated by reactive deposition epitaxy on Si(111) substrates. We should additionally note that this approach provides the ability to reliably control the areal density, size, and crystalline phase of the nanodots, avoiding metastable phases commonly observed in iron silicide nanostructures and thin films.^{15,16} In particular, a change in phase formation from ϵ -FeSi to β -FeSi₂ nanodots as a function of the deposited amount of iron (θ_{Fe}) was examined by atomic force microscopy (AFM) and x-ray diffraction (XRD).

The samples were prepared in an ultrahigh vacuum (UHV) evaporation system at a base pressure of about 1×10^{-9} Torr by RDE. Prior to the growth process, the Si(111) substrates were hydrogen passivated¹⁴ to assure an atomically flat and clean silicon surface terminated by hydrogen atoms. The substrates were then introduced into the UHV chamber and heated at 400 °C for 30 min for degas-

ing. The temperature of the substrates was then raised to 700 °C and an iron film (99.999% of purity) with a nominal thickness θ_{Fe} was deposited at a rate of 0.06 nm/s as measured by a quartz crystal oscillator. After deposition, the samples were annealed at 700 °C for two hours in UHV. Twelve different samples where grown with iron coverage between $\theta_{\text{Fe}}=2.0$ nm and $\theta_{\text{Fe}}=12.0$ nm. The morphological evolution of the samples as a function of θ_{Fe} , was examined by AFM using TappingMode™ in a Veeco MultiMode scanning probe microscope with a NanoScope IV controller. The structural properties of the samples were also investigated by XRD. The diffraction experiments were carried out at beam-line XRD1 of the Brazilian Synchrotron Light Laboratory (LNLS, Campinas, SP) at 10.0 keV x-ray photon energy ($\lambda=1.24$ Å).

Figure 1 shows the morphology of three samples with (a) $\theta_{\text{Fe}}=2.4$ nm, (b) $\theta_{\text{Fe}}=3.8$ nm, and (c) $\theta_{\text{Fe}}=5.5$ nm. At low θ_{Fe} hemispherical iron silicide nanodots are formed, increasing in size and density as θ_{Fe} increases. At $\theta_{\text{Fe}} \sim 5.5$ nm the iron silicide nanodots completely cover the surface of the sample and their areal density reaches a maximum value of approximately 10^{11} cm⁻² before nanodots coalescence begins to set in. At larger θ_{Fe} the density of nanodots decreases and large iron silicide islands are created.

A closer look at the AFM images of Figs. 1(a)–1(c) shows that in fact two families of nanodots are present in the samples. The first family is formed by small and low aspect ratio (defined here as the volume to base area ratio) nanodots, while the second family consist of larger nanodots with high aspect ratio. This behavior can be observed in Fig. 1(d)–1(f) where a statistical analysis of nanodots volume versus base area is presented. At low θ_{Fe} most of the nanodots are small and present a low aspect ratio. However, as θ_{Fe} increases the population of larger and high aspect ratio nanodots also increases. At $\theta_{\text{Fe}}=5.5$ nm almost all nanodots have a high aspect ratio. The mean aspect ratio of the low and high aspect ratio families of nanodots is 0.7 and 3.5 nm, respectively. Therefore, for a more intuitive interpretation of the aspect ratio plots, and without introducing any significant distortion, an aspect ratio threshold of 1 nm was chosen to differentiate the two families of nanodots. The mean volume as well as the standard deviation of the volume of the nan-

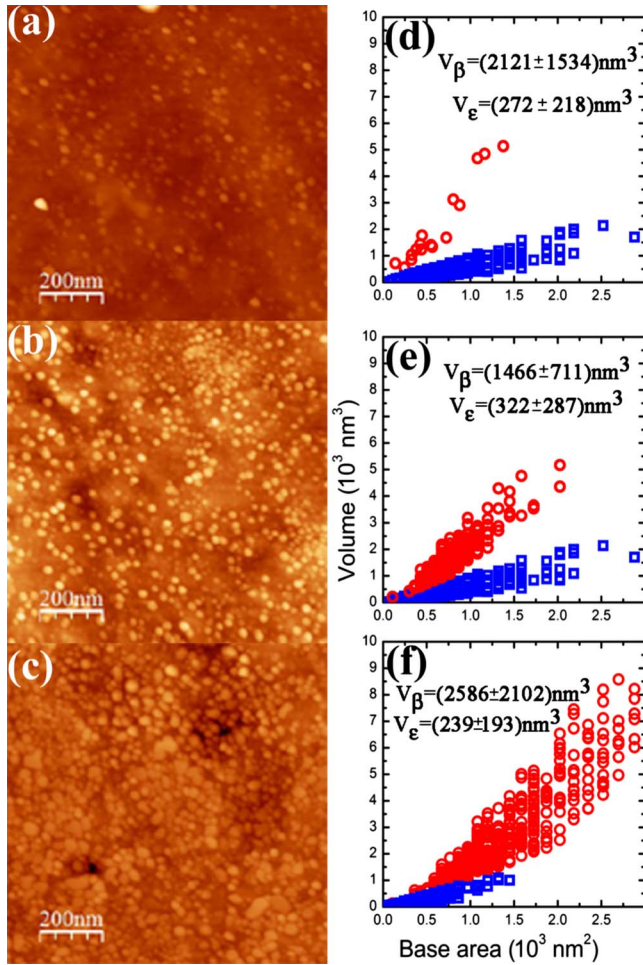


FIG. 1. (Color online) AFM images of samples with (a) $\theta_{Fe}=2.4$, (b) 3.8, and (c) 5.5 nm. Statistical analysis of the AFM images of the samples with (d) $\theta_{Fe}=2.4$, (e) 3.8, and (f) 5.5 nm. The nanodots with aspect ratio lower than 1 nm were denoted by open blue squares, while the nanodots with aspect ratio larger than 1 nm have been denoted by open red circles.

odots of each phase is also shown in Figs. 1(d)–1(f).

In order to understand the shape transition presented in Fig. 1 the structural properties of selected samples were studied by XRD measurements in reflection geometry. Figure 2 shows two typical diffractograms of low and high iron coverage samples. Both samples are polycrystalline with a mixture of ϵ -FeSi and β -FeSi₂ phases. However, a strong texture was observed in all samples with the ϵ -FeSi(111)/Si(111), β -FeSi₂(220)/Si(111), and β -FeSi₂(202)/Si(111) heteroepitaxial relationships. Due to the small difference between the *b* and *c* lattice constant of the orthorhombic β -FeSi₂ and to the shift and broadening of the Bragg peaks caused by the strain and small size of the nanodots, it is very difficult to distinguish between the two heteroepitaxial β -FeSi₂/Si relationships in our diffractograms. Therefore we use a β -FeSi₂(220)/(202) notation in the following to indicate that fact. In addition to the ϵ -FeSi and β -FeSi₂ phases no other iron silicide phases were observed. This result contrasts with common observations of the formation of metastable iron silicide phases prior to β -FeSi₂.^{15,16}

The XRD data were analyzed to infer the concentration of

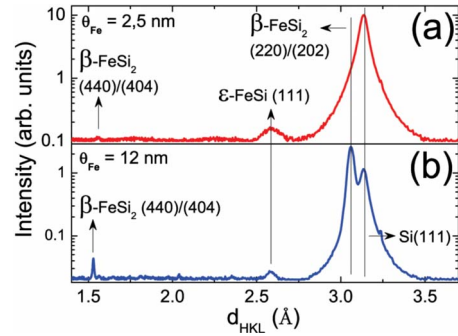


FIG. 2. (Color online) Typical XRD diffractograms of (a) low and (b) high iron coverage samples. The measurements were performed in reflection geometry and a small beam divergence of 0.005° was used to avoid an overlap of the substrate signal. Therefore, all linewidths of peaks stemming from the nanodots can be inferred directly from the diffraction data, without the need of instrumental deconvolution.

each phase in the samples, as well as the average grain size and strain of the crystallites along the growth direction. The concentration of each phase was calculated following the standard procedure described in Ref. 17. It was considered that only the ϵ -FeSi and β -FeSi₂ phases were present in the samples. The effects of absorption, texture, multiplicity and Lorentz-polarization factor in the intensity of the Bragg peaks were also taken into account. The strain in the dots was estimated by comparing the lattice distance of the ϵ -FeSi(111) and β -FeSi₂(220)/(202) reflections with the respective bulk values. The Scherrer equation¹⁷ was used to infer the evolution of the grain size along the growth direction as a function of θ_{Fe} .

Figure 3 shows the results of the analysis of the XRD data. The relative concentration of the iron silicide phases are

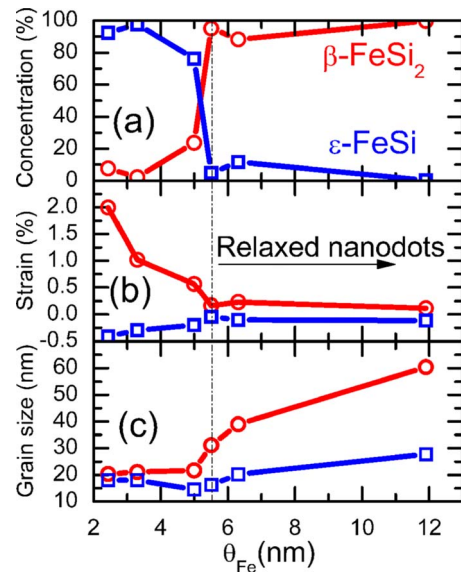


FIG. 3. (Color online) Analysis of the XRD data as a function of θ_{Fe} : (a) relative concentration of the ϵ -FeSi and β -FeSi₂ phases, (b) strain along the growth direction, and (c) grain size along the growth direction.

shown in Fig. 3(a) as a function of θ_{Fe} . The most striking feature of this graph is a clear phase transition from the ε -FeSi to β -FeSi₂ at approximately $\theta_{\text{Fe}}=5.5$ nm, coinciding with the coalescence process observed in the AFM images. A clear relaxation of the strain can also be observed at $\theta_{\text{Fe}}=5.5$ nm followed by a sharp rise of the β -FeSi₂ grain size. This coverage is also the optimum value to obtain samples with a large density of almost single phase (95% of the material in the β phase) and small (mean size around 30 nm) β -FeSi₂ nanodots. The grain size analysis also show that both phases present different mean crystallites sizes, being the ε -FeSi smaller than the β -FeSi₂ crystallites. These results show that the two families of nanodots observed in the AFM images not only correspond to nanodots of different shape and sizes, but also of different crystallographic phases and chemical composition. Based on the evolution of the ε -FeSi and β -FeSi₂ phase concentrations and grain sizes as θ_{Fe} increases, it is possible to identify the family of smaller and low aspect ratio nanodots as being of the ε -FeSi phase and the family of larger and high aspect ratio ones as being of the β -FeSi₂ phase.

The AFM and XRD results indicate that for small nanodots the relaxation of the strain in the nanodots should be the driving force for the phase transition. It is interesting to note that the phase transition sequence ε -FeSi \rightarrow α -FeSi₂ \rightarrow β -FeSi₂, sometimes intercalated by several metaestable phases, frequently observed as a function of the increasing iron coverage for high annealing temperatures (>500–700 °C) in iron silicide thin films^{18,19} is not present in our samples. The availability of Si adatoms from the substrate to form Si-rich iron silicide phases, usually invoked to explain phase transitions in iron silicide thin films,¹⁹ is also not an issue here since the growth and annealing temperatures are high enough to sustain a large Si and Fe diffusion and the β -FeSi₂ (Si-rich phase) was observed to be formed mostly in the thicker samples. Our phase transition follows more closely the iron-silicon bulk phase diagram²⁰ with a direct ε -FeSi \rightarrow β -FeSi₂ transition.

From the thermodynamic point of view the ε -FeSi \rightarrow β -FeSi₂ transition can be qualitatively understood in a similar way to the shape transitions observed in self-assembled strained islands,^{21–24} where a competition between the increase in surface energy due to the creation of a

wetting layer and the decrease in the island energy due to elastic relaxation determines not only a thermal energy barrier for the island nucleation but also the transition to lower energy shapes. However, in our case of nonwetting nanodots the increase in surface energy due to the nanodot-substrate interface has to be considered. Considering a simple model of pyramidal shaped islands the energy excess necessary to create a faceted island is^{22–24}

$$\Delta E = 2 \left[\frac{3}{2} \cot(\alpha) \right]^{1/3} V^{1/3} [\gamma_l \cos(\alpha) - \gamma_s] - 6 \frac{\sigma_{xx}^2 (1 - \nu^2)}{\pi E} V \tan(\alpha). \quad (1)$$

Were V is the volume of the island, α is the angle between the island facets and the substrate surface, E is the Young's modulus of the island, ν is the Poisson's ratio of the island, σ_{xx} is in-plane stress of the island due to the lattice mismatch with the substrate, γ_l is the elastic energy per unit area of the island facet, and γ_s is the interface energy per unit area of the island interface with the substrate.

The first term of the right side of the above equation refers to the increase in surface and interface energy due to the creation of the island and the second term refers to the elastic energy relaxation in the island. As the volume of the island increases the excess energy increases reaching a maximum that corresponds to the energy barrier for nucleation of the island at a critical volume V_c . For $V > V_c$ the excess energy decreases due to the elastic relaxation. As θ_{Fe} increases the elastic relaxation of the high aspect ratio and lower lattice mismatch ($\delta=1.4\%$ along the b axis of the orthorhombic unit cell and $\delta=1.95\%$ along the c axis) β -FeSi₂ nanodots must be more effective in lowering the nanodots excess energy that in the case of the low aspect ratio and higher lattice mismatch ($\delta=4.3\%$) ε -FeSi nanodots. At some particular volume, larger than V_c for each phase, the excess energy of the ε -FeSi island will be equal to the excess energy of the β -FeSi island. At this cross point there is a discontinuity in the chemical potential²² promoting from this point up the growth of the β -FeSi₂ nanodots at the expense of the ε -FeSi nanodots. The volume V_T of the islands at this transition point is

$$V_T = \left(\frac{\left[\frac{3}{2} \cot(\alpha_2) \right]^{1/3} [\gamma_{l2} \cos(\alpha_2) - \gamma_{s2}] - \left[\frac{3}{2} \cot(\alpha_1) \right]^{1/3} [\gamma_{l1} \cos(\alpha_1) - \gamma_{s1}]}{3 \frac{\sigma_{xx2}^2 (1 - \nu_2^2)}{\pi E_2} \tan(\alpha_2) - 3 \frac{\sigma_{xx1}^2 (1 - \nu_1^2)}{\pi E_1} \tan(\alpha_1)} \right)^{3/2}, \quad (2)$$

Were the subindex 1 and 2 correspond to the ε -FeSi and β -FeSi₂ islands, respectively. The transition volume corresponds to the largest possible volume of the ε -FeSi islands at the equivalent iron coverage of approximately 5.5 nm. A

direct look to the AFM data presented in Fig. 1 reveals that the maximum volume of the ε -FeSi islands in our samples is approximately 2000 nm³. Unfortunately, a further comparison of the model with the experimental results needs values

for γ_1 , γ_s , E , and ν , for both phases, that are not well known. This process can be further accelerated by the presentation of dislocations in the β -FeSi₂ nanodots that will reduce, even more, the excess energy of the nanodots. Regardless of other kinetics aspects, in this coarsening, large β -FeSi₂ nanodot grow while ε -FeSi nanodots shrink and disappear. Furthermore, since the phase transition is largely accelerated at the onset of nanodots coalescence and of large elastic relaxation kinetics aspects and interaction between the nanodots could also play also an important role in the transitions. The observation of a variety of different morphologies for nanodots of approximately the same volume reinforces this conclusion.

In summary, it is shown that almost single phase ε -FeSi and β -FeSi₂ iron silicide nanodots can be formed by reactive deposition epitaxy on Si(111). The density, size, and shape of the nanodots can be controlled by the amount of deposited iron. However, low iron coverage leads to ε -FeSi reach samples with small islands, while high iron coverage leads to

β -FeSi₂ reach samples with large ones. A direct comparison of the diffraction and microscopy data shows that nanodots of each phase exhibit different shapes, being the ε -FeSi (β -FeSi₂) nanodots of a low (high) aspect ratio. The ε -FeSi to β -FeSi₂ transition is observed at iron coverage of 5.5 nm and is coincident with the coalescence of the nanodots, the relaxation of the strain in both phases and a steep increase of the grain size of the β -FeSi₂ phase. This coverage was found to be the optimum to obtain almost single phase samples with a large density of small β -FeSi₂ nanodots. A thermodynamic qualitative model to explain the phase and shape transitions was also discussed. Several kinetics issues and facts that can play an important role in the transitions were also pointed out.

We would like to thank the Brazilian National Light Synchrotron Laboratory, CNPq, CAPES, and FAPEMIG for the financial and technical support of this work.

-
- ¹A. Vantomme, M. A. Nicolet, G. Bai, and D. Fraser, *Appl. Phys. Lett.* **62**, 243 (1993).
- ²K. Lefki and P. Muret, *J. Appl. Phys.* **74**, 1138 (1993).
- ³M. Takeda, M. Kuramitsu, and M. Yoshio, *Thin Solid Films* **461**, 179 (2004).
- ⁴D. Leong, M. Harry, K. J. Reeson, and K. P. Homewood, *Nature (London)* **387**, 686 (1997).
- ⁵Z. Liu, S. Wang, N. Otagawa, Y. Suzuki, M. Osamura, Y. Fukuzawa, T. Ootsuka, Y. Nakayama, H. Tanoue, and Y. Makita, *Sol. Energy Mater. Sol. Cells* **90**, 276 (2006).
- ⁶A. Rizzi, B. N. E. Rösen, D. Freundt, C. Dieker, H. Lüth, and D. Gerthsen, *Phys. Rev. B* **51**, 17780 (1995).
- ⁷J. E. Mahan, V. L. Thanh, J. Chevrier, I. Berberzier, J. Derrien, and R. G. Long, *J. Appl. Phys.* **74**, 1747 (1993).
- ⁸T. Miki, Y. Matsui, K. Matsubara, and K. Kishimoto, *J. Appl. Phys.* **75**, 1693 (1994).
- ⁹Q. Zhang, M. Tanaka, M. Takeguchi, M. Han, and K. Furuya, *Jpn. J. Appl. Phys., Part 1* **42**, 4667 (2003).
- ¹⁰Y. Ozawa, T. Ohtsuka, C. Li, T. Suemasu, and F. Hasegawa, *J. Appl. Phys.* **95**, 5483 (2004).
- ¹¹A. Wohlleben, B. Hollander, S. Mesters, C. Dieker, G. Creelius, W. Michelsen, and S. Mantl, *Thin Solid Films* **287**, 93 (1996).
- ¹²T. Suemasu, Y. Negishi, K. Takakura, F. Hasegawa, and T. Chikyow, *Appl. Phys. Lett.* **79**, 1804 (2001).
- ¹³D. R. Miquita, R. Paniago, W. N. Rodrigues, M. V. B. Moreira, H. D. Pfannes, and A. G. de Oliveira, *Thin Solid Films* **493**, 30 (2005).
- ¹⁴D. R. Miquita, J. C. González, M. I. N. da Silva, W. N. Rodrigues, M. V. B. Moreira, R. Paniago, R. Ribeiro-Andrade, R. Magalhães-Paniago, H. D. Pfannes, and A. G. de Oliveira, *J. Vac. Sci. Technol. A* **26**, 1138 (2008).
- ¹⁵J. Won, A. Kovács, M. Naito, M. Ishimaru, and Y. Hirotsu, *J. Appl. Phys.* **102**, 103512 (2007) and references cited therein.
- ¹⁶I. Dézsi, Cs. Fetzter, I. Szücs, J. Dekoster, A. Vantomme, and M. Caymax, *Surf. Sci.* **599**, 122 (2005), and references therein.
- ¹⁷*Thin Film Analysis by X-Ray Scattering*, edited by Mario Birkholz, Paul F. Fewster, and Christoph Genzel (Wiley-VCH Verlag GmbH & Co. KGaA, Weinheim, 2006).
- ¹⁸H. Nakano, K. Maetani, K. Hattori, and H. Daimon, *Surf. Sci.* **601**, 5088 (2007).
- ¹⁹K. Kataoka, K. Hattori, Y. Miyatake, and H. Daimon, *Phys. Rev. B* **74**, 155406 (2006) and references therein.
- ²⁰M. Hansen, *Constitution of Binary Alloys* (McGraw-Hill, New York, 1958).
- ²¹I. Daruka, J. Tersoff, and A. L. Barabasi, *Phys. Rev. Lett.* **82**, 2753 (1999) and references therein.
- ²²F. M. Ross, J. Tersoff, and R. M. Tromp, *Phys. Rev. Lett.* **80**, 984 (1998).
- ²³J. Tersoff and F. K. LeGoues, *Phys. Rev. Lett.* **72**, 3570 (1994).
- ²⁴K. Brunner, *Rep. Prog. Phys.* **65**, 27 (2002).